Accepted Manuscript

Authors: Adeel S Shafi, Jake McClements, Ibrahim Al-Baijan, Radwa H. Abou-Saleh, Carmel Moran, Vasileios Koutsos
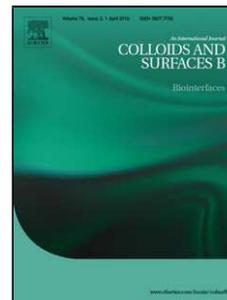
Please cite this article as: Shafi AS, McClements J, Al-Baijan I, Abou-Saleh RH, Moran C, Koutsos V, Probing Phospholipid-Microbubbles by Atomic Force Microscopy to Quantify Bubble Mechanics and Nanostructural Shell Properties, *Colloids and Surfaces B: Biointerfaces* (2019), https://doi.org/10.1016/j.colsurfb.2019.04.062

This is a PDF file of an unedited manuscript that has been accepted for publication. As a service to our customers we are providing this early version of the manuscript. The manuscript will undergo copyediting, typesetting, and review of the resulting proof before it is published in its final form. Please note that during the production process errors may be discovered which could affect the content, and all legal disclaimers that apply to the journal pertain.

Probing Phospholipid-Microbubbles by Atomic Force Microscopy to Quantify Bubble Mechanics and Nanostructural Shell Properties

Adeel S Shafi[†‡], Jake McClements[†], Ibrahim Al-Baijan[†], Radwa H. Abou-Saleh[§š], Carmel Moran[‡], Vasileios Koutsos[†,*]

[†] School of Engineering, Institute for Materials and Processes, The University of Edinburgh, The King's Buildings, Edinburgh EH9 3FB, United Kingdom

[‡] Centre for Cardiovascular Science, Queen's Medical Research Institute, The University of Edinburgh, Edinburgh EH16 4SB, United Kingdom

[§] Molecular and Nanoscale Physics Group, School of Physics and Astronomy, University of Leeds, LS2 9JT, United Kingdom

[š] Biophysics Group, Department of Physics, Faculty of Science, Mansoura University, Egypt

*Correspondence should be addressed; Email: vasileios.koutsos@ed.ac.uk; Tel.: +44 (0)131 6508704

Graphical_abstract
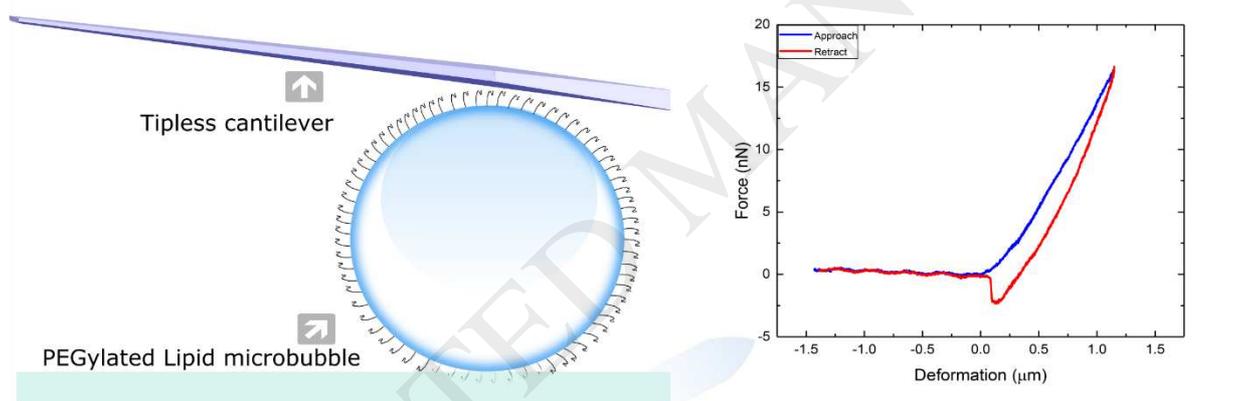
Highlights

- Using tapping mode imaging, the thickness of microbubble shells can be quantified
- Quantifying shell thickness has significant impact on Young's Modulus values
- Atomic force microscopy can be used to quantify thickness of the PEG brush layer

ABSTRACT: Microbubbles (MBs), which are used as ultrasonic contrast agents, have distinct acoustic signatures which enable them to significantly enhance visualisation of the vasculature. Research is progressing to develop MBs which act as drug/gene delivery vehicles for site-specific therapeutics. In order to manufacture effective theranostic vehicles, it is imperative to understand the mechanical and nanostructural properties of these agents; this will enrich the understanding of how the structural, biophysical and chemical properties of these bubbles impact their functionality. We produced microfluidic phospholipid-based MBs due to their favourable properties, such as biocompatibility and echogenicity, as well as the ability to modify the shell for targeting applications. We have drawn upon atomic force microscopy to conduct force-spectroscopy and tapping-mode imaging investigations. We have, for the first time to our knowledge, been able to accurately quantify the thickness and lipid configuration of phospholipid-shelled MBs - showing a trilayer as opposed to the conventional monolayer structure. Furthermore, we have measured MB stiffness and employed different mechanical theories to quantify the Young's Modulus. We show that the Reissner theory is inappropriate for mechanical characterisation of phospholipid MBs, however, the Hertz model does offer biologically relevant comparisons. Analysis using the Alexander-de Gennes polymer brush theory has allowed us to provide new information regarding how the thickness of the polyethylene glycol brushes, end-grafted to our phospholipid microbubbles, changes with diameter.

Keywords: Atomic force microscopy

Statistical Summary

Total number of words: 7621
Total number of figures: 9

Introduction

Ultrasound (US) imaging is a real-time imaging technique which allows visualisation of organ structure. It is non-invasive, more economical than other imaging modalities and does not produce any ionizing radiation. The strength of the received scattered signal dictates the level of grey-scale contrast seen on the US image. Blood is a poor scatterer of US and interpretation of the images produced has long been a limitation of its use, especially within the vascular context. To further enhance image acquisition from US, contrast agents, known as microbubbles (MBs) are used. These are micron sized bubbles (1-8 µm) made of biocompatible, biodegradable shell material which encapsulate a gas core, this increases the image contrast due to the acoustic mismatch between the gas and the surrounding vascular structures. This has opened multiple avenues for both diagnostic and molecular imaging purposes (1–4).

In the biomedical setting, the composition, mechanical and nanostructural properties of MBs shells are being studied extensively using a variety of methodologies. These include acoustic investigations using high frequencies (5,6), to optical investigations using micropipette aspiration (7) and optical tweezers in line with ultra-high speed cameras (8). The importance of understanding the mechanics of the biocompatible bubbles is due to the fact that once inside the body there are many physiological challenges the MB will face; pulmonary filtration, blood pressure, alteration of the internal gas concentration due to diffusion, as well as thermal changes impacting mechanical integrity as they pass to the desired region of interest (9). It is for this reason that first generation shell-free MBs are no longer used, surface tension at the gas-liquid interface causes dissolution of the bubble, and therefore the free-MB will dissolve spontaneously and almost instantly. Soft-

shell MBs are coated in thin layers of molecules such as palmitic acid or phospholipids (10) whereas hard-shell MBs are more robust and are encapsulated in material which has less compliance and echogenicity, such as polylactide and albumin (11). To be used as biomaterials for enhancing therapeutics and diagnosis, these parameters are important not only in application, but also for long shelf-life (days to months) (10). Currently third generation microbubbles are in use. These agents improve stability by incorporating denser insoluble gases in to the core as well as additional modification of the shell; commonly a phospholipid variation which is end-grafted to polyethylene glycol (PEG), or other hydrophilic compounds. These PEGylated MBs can avoid aggregation and improve invisibility from the immune system (12). Further chemical and physical modifications of the shell allow for the incorporation of bioactive molecules and particles, namely nanoparticles, antibodies and even drug carriers such as liposomes for molecular imaging purposes (13–15). For our MBs to be used as not only reliable contrast agents, but for highly effective therapeutic delivery vehicles, we deliberately incorporated a polyethylene glycol (PEG) layer. PEG is an inert, water-soluble polymer which, over the last two decades, has become essential in the design and manufacture of biocompatible agents. Steric repulsion makes the polymeric chains protrude perpendicularly from the surface of the membrane to which they are grafted. Consequently, they can then provide invisibility from the immune system as they create a barrier which prevents adhesion to pathogenic-detecting components within the vasculature, thus, increasing biocompatibility whilst decreasing MB-coalescence (16). We have opted for the development and characterisation of a soft-shelled, PEGylated-phospholipid microbubble.

When sonicated, the absorption of the sonic energy causes the MBs to oscillate. An oscillating MB contracts and expands as a result of the positive and negative pressure of the ultrasound-pulse-wave. In comparison to a free bubble of similar size, the addition of a shell causes the resonance frequency of the MB to increase; meaning a higher acoustic frequency is required to cause resonant oscillations compared to a shell-free MB (17–19). The ability to detect MBs in the in-vivo clinical setting is dependent on the MB shell parameters, such as shell thickness and stiffness (20).

Since its introduction over thirty years ago (21), atomic force microscopy (AFM) has become a versatile and highly quantitative experimental technique capable of capturing lateral resolution of the order of nanometres, vertical resolution of the order of Angstroms and force resolution as accurate as 10 piconewtons (22–24). It is fast becoming one of the most important tools in the biomedical setting. It can provide nanoscale resolution of topographical data in liquids, and observe highly sophisticated molecular interactions that offer information on how biomaterials (and cells) change their structural, biophysical and chemical properties to adjust their functionality (25–27). The unprecedented resolution in the liquid environment of this scanning probe microscope makes it the ideal tool for the quantification of mechanical and nanostructural properties of the MB shell (28).

To quantify the mechanical and nanostructural parameters highlighted above, AFM has been validated for investigations on phospholipid-based MBs (29) and also to image MB specific binding (14). With further work using the AFM to investigate different shell modifications and different coatings on the MB shell (30,31). The investigations discussed here have highlighted the importance of MB shell structure and composition and how they strongly influence the mechanical properties as well as their acoustic response when sonicated. However, further characterisation is required, particularly in quantifying domain structure and thickness of the shell. Through understanding the structure and size of the shell membrane, the data acquired can be used within the mathematical theories currently used when analysing data produced from AFM-MB experiments, such as the Reissner and Hertz models. Currently conjectural values are used for MB shell thickness in these models. Being able to quantify this will significantly enhance the consistency of the AFM data. Furthermore, most MB formulations today incorporate PEG within the membrane (32). AFM investigations from Radwa et al. have shown how increasing the concentration of PEG, which is end-grafted within the shell membrane, causes a change in configuration from mushroom to brush (33), however,

experimental data highlighting the homogeneity of the grafting and the actual thickness of the brush layer in MBs that are in their original state remains elusive.

Henceforth, in this paper, we used AFM to address these questions through tapping mode imaging to accurately quantify MB shell thickness. We continued with the AFM and used force indentation-curves to further quantify MB mechanical shell properties through different mathematical theories, which also provided new information on which were best suited to AFM-MB investigations. Such as employing the classical Hertz theory that treats the MB as a homogenous microsphere, rather than the Reissner theory which we found to over-estimate the Young's Modulus for soft-shelled MBs. Furthermore, novel analysis of the AFM data using the Alexander-de Gennes theory of a polymer brush enabled us to provide new information regarding the PEG brush that protrudes from the MB shell.

Experimental

Materials

The lipids used throughout this investigation are 1, 2-dipalmitoyl-sn-glycero-3-phosphocholine (DPPC) and 1, 2-distearoyl-sn-glycero-3-phosphoethanolamine-N-[amino (polyethylene glycol)-2000] (DSPE-PEG$_{2000}$). Lipids were purchased from Avanti Polar Lipids (Alabaster, AL). Glycerol (Sigma-Aldrich, St Luis, MO). Perfluorobutane (C_4F_{10}) formulated the gaseous core of MBs.

Microbubble Preparation

Using the method previously described (34); Lipids were mixed together at a 95% DPPC and 5% DSPE-PEG$_{2000}$ molar ratio in a glass vial, then dried down under a steady stream of Nitrogen to dry off the solvent. The dried lipid film was then resuspended in 1 ml of prepared buffer solution (4mg/ml NaCl +1% Glycerol). The mix was vortexed for one minute to allow for the occurrence of a turbid appearance (lipids had suspended in the buffer solution at this point). The glass vial was then placed in a sonic bath (VWR Ultrasonic Cleaner, Leicestershire, UK) for one hour, whilst being vortexed every ten minutes. This reduced the volume of random errors during MB-manufacture as this practice accounts for the possibility of, and eliminates, micelles and other large aggregates (35). After sonication, 10 µl of tetradecafluorohexane (C_6F_{14}) was added to the solution as it effectively results in the saturation of the surrounding medium, reducing the ability of C_4F_{10} gas to partition into the aqueous phase (36). The lipid suspensions were vortexed, then cooled for 15 minutes at 4°C prior to microfluidic production using the microfluidic system (Horizon v2.2, Leeds, U.K, Patent no 9802165) (34,37). MBs were produced using a microspray regime whereby gas pressure was 20 Psi and liquid flow rate was 60 µl/min.

For sizing and concentration studies of our MB sample, a 10 µl sample was collected from the middle of the MB solution and was diluted 10-fold. From this diluted sample, 30 µl was taken from the middle of the MB solution and inserted into a 50 µm depth chamber on a glass slide. MBs were then allowed to rise for ~2 minutes before optical microscopy images were collected. An inverted microscope (Axiovert 135M, Carl Zeiss, Germany) was used to image the MBs using a 40x magnification. 38 images were captured using the Jenoptik Progres Gryphax Subra Digital Camera System (Jenoptik, Germany) attached to the microscope. Images were analysed using ImageJ freeware (https://imagej.nih.gov/ij/) to obtain size distribution and concentration. Data produced from ImageJ was statistically analysed using Origin Pro (version 8.5 or later).

For AFM experiments, individual MB sizing was conducted using the inverted optical microscope, Nikon TE2000U (Nikon UK Limited, Surrey, UK) attached to the atomic force microscope (MFP-1D, Asylum Research, Santa Barbara, CA, USA).

AFM Tapping Mode Imaging

MBs were manufactured using the same methodology described above. However, to eliminate the presence of any other chemicals on the surface, MBs were suspended in 1 ml of deionised water (18.2 MΩ-cm), as opposed to the usual buffer solution [4 mg/ml NaCl and 1% glycerol] used for the force-curve investigations. Prior to imaging, MBs were diluted down to a 1:10 concentration, and then approximately 20 µl of the diluted MB solution was placed on the centre of the mica surface. This was then incubated in a vacuum oven at 40°C for a period of 20 hours. This was adequate time to remove any excess water, yet leave behind, on the strongly hydrophilic mica, a thin film of water which the phospholipid remnants would be immersed in due to their hydrophilic nature. In fact, although we image the MB remnants in macroscopically "dry" conditions on mica, mica is hydrophilic and retains an ultrathin layer of water (38).

All AFM imaging was carried out under ambient conditions in air using a Bruker Multimode/Nanoscope IIIa instrument (Bruker, Santa Barbara, Ca, USA). A J-scanner was used for the imaging which had an x-y range of ~160 µm. RTESPA model cantilevers were purchased from Bruker with a nominal tip radius of 8 nm, nominal spring constant of 40 N/m and nominal resonant frequency of 300 kHz. During imaging, the scan rate was kept relatively low with a frequency of approximately 0.3 Hz. All analysis of the images were carried out using Gwyddion data analysis software, v2.8 (open-source software for SPM data analysis) (39), to quantify shell-thickness.

AFM Force-Curves

Surface Preparation

As demonstrated before (29), prospective MB samples were immobilised on the surface in such a manner that structural and mechanical integrity was upheld. Petri-dishes used, Greiner CellStar® (Greiner Bio-One GmbH, Germany) were coated in Poly-L-Lysine (Sigma-Aldrich Co. St Louis, MO) to create cationic surface regions throughout the dish. The dish was then inverted and placed in a large suspension of deionised water (18.2 MΩ-cm) which contained the MBs for 16 minutes. The dish was turned 90° every four minutes to allow maximum rates of adhesion of MBs to the dish surface. Due to the MBs being buoyant (34), they would float and this encouraged them to adhere to the dish. This process, which ensured MBs were always wetted, reduced the likelihood of structural or mechanical damage.

Once the preparation process had been completed, the Greiner CellStar® (Greiner Bio-One GmbH, Germany) petri-dish which now contained immobilised MBs would be filled up to 75% of its capacity, in physiologically representative saline solution.

Force Measurements

Force curves were collected using the AFM MFP-1D (Asylum Research, Santa Barbara, CA, USA). The MFP-1D is mounted on an inverted optical microscope (Nikon TE2000-U, Nikon UK Limited, Surrey, UK) and attached to a digital camera (Orca – ER C4742-80, Hamamatsu Photonics, Japan). The tipless cantilevers used were silicon-made, aluminium-back-coated cantilevers (NSC12/Tipless/AIBS, MikroMasch, Tallinn, Estonia). Spring constants (k_c) were calibrated using the thermal tuning method (40) and ranged between 0.19 and 0.29 N/m. The digital camera allowed for the use of live image processing through the analysis software, IP Lab v3.7, (BD Bioscience Bioimaging, Rockville, MD). This allowed for determination of MBs diameter (D) within an accuracy of $\pm$ 0.5 µm.

The cantilever was always placed at a distance of 3 µm. This distance ensured there were no disturbances of MB and/or cantilever during set-up. The scan rate was 0.5 Hz for all investigations. The relatively low frequency used, a value which represents the number of 'trips' the cantilever makes to and from the sample

per second, minimised structural disturbances as the MBs were being compressed in a quasi-static process. Once the MBs had been sized, the cantilever was positioned at the pole of the MB and then 30 sets of data were collected from each MB to ensure reproducibility. The MBs would be analysed optically and qualitatively to ensure they had not become immobilised and/or been permanently deformed, ensuring data collected was evaluating bubble elasticity and not bubble plasticity.

During the compression of MBs, the aligned laser would deflect upon the quadrant photodiode receptor and generate raw data in the form of piezoelectric displacement vs. cantilever deflection. The values collected would be treated mathematically to determine the compressive force, F (nN), and the deformation, Δ (μm), of the MB during each compression. Deformation of the MB is quantified by finding the difference between the piezoelectric displacement and cantilever deflection, while the compressive force applied on the MB was quantified by applying Hooke's law (28) where δ is the cantilever deflection and k_c is the cantilever spring constant:

$$F = \delta k_c \qquad (1)$$

The nano-manipulation of the raw AFM-data to measure compression force relative to sample deformation allows for further analysis to quantify the mechanical properties of the MBs.

Results & Discussion

Optical Investigation

Using microfluidic technology to produce our MBs, optical microscopy images were obtained and MB concentration was calculated to be 4.8×10^8 MBs/ml with an average diameter of 3.6 ± 2.8 μm.
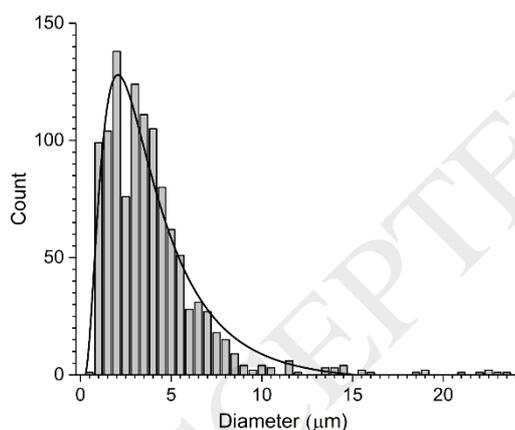

Figure 1. Histogram representing the size distribution of our MBs calculated using brightfield microscopy.

Tapping Mode Imaging of Shell Remnants in Air

To quantify the thickness (t) of the MB shell, we removed excess water from the MB sample by placing the samples in a vacuum oven, and then imaged the remnants using tapping mode AFM. Figure 2 shows typical AFM height images taken from various sections of the samples, at a dilution of 1:10. Images in Figure 2a and 2b clearly show material on different areas on the surface, the black line in figure 2a represents imaging of a multi-layered surface, whereas the green line in figure 2b represents imaging of a single layered surface. In figure 2c we can see representative line scans that correspond with the black and green lines on figure 2a and 2b - that show fixed height profiles.
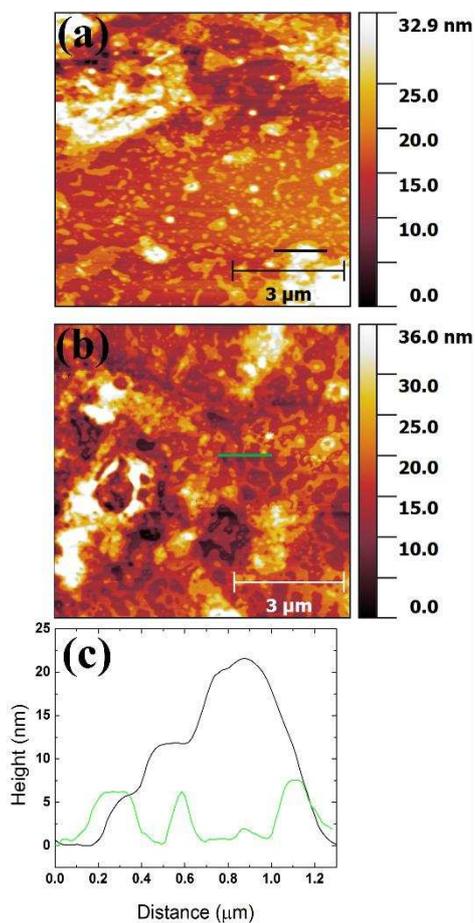
Figure 2. Tapping mode AFM height images. (a) and (b), images showing the remnants of MBs shells on a mica surface after excess deionised water was removed by placing samples in a vacuum oven; (c) two representative height profiles of single and multilayers (corresponding to the horizontal lines in fig 1a and 1b).

The shell remnants formed asymmetrical features that appeared to have fixed height values. Additionally, the features could form layers on top of one another creating terraced structures.

Figure 3 displays a histogram showing the height distribution of the phospholipid layers. The distribution exhibits a distinct peak and an average height of 6.3 ± 0.7 nm.
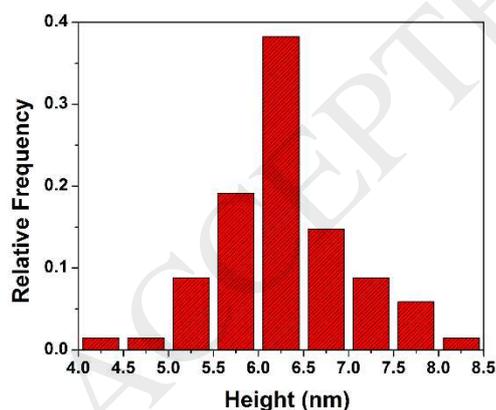
Figure 3. Histogram showing the height distribution of single MB layers on a mica surface, imaged using tapping-mode. Note the distinct peak at 6.3 nm, taken from 68 measurements.

DPPC; the same lipid constituting 95% of our MB-membrane formulation, is one of the most popular lipids studied, alongside DMPC, DOPC, EPC and DLPE. Despite lipids being vital components for structure and function of biological cells, as well as now being used as surfactants to combat surface tension for biocompatible particles, such as for the in-house MBs used in this study, there are still academic challenges that remain when investigating such lipids; much of that difficulty is obtaining appropriate quantitative structural information while samples are in their natural hydrated state, especially for biological relevant understanding (41,42). Questions regarding parameters such as membrane thickness, charge density and

numerical values for area per molecule remain of interest. (43,44). Prior to the development of AFM, x-ray scattering was used to determine the thickness of the hydrophobic-tailed region of pure lipid bilayers forming phospholipid vesicles. A linear relationship was shown to exist between the number of carbons and thickness of bilayer. The thickness ranged from ~ 1 to 4 nanometres on average as the number of carbons across the hydrophobic region increased from around 10 to 40 (45). Nagle et al.(42) was able to show in later years that the hydrophilic head-region has a thickness of ~ 1 nm. This data on lipid bilayers suggest that bilayer thickness for 40-carbon phospholipids (as the ones used in our study) is ~ 5 nm. Using similar methodology to our present study, Unsay et al(45) showed through tapping-mode imaging there was a height distribution of ~ 4 nm on supported lipid bilayers. We have shown an average membrane thickness of 6.3 nm, despite the consensus that phospholipid-MBs are stabilised by a monolayer formulating the membrane (46). The increase in our thickness values, compared with thickness readings on bilayers, leads us to propose MB membranes could be tri-layered; undertaking a {hydrophilic head-hydrophobic tail}-{hydrophobic tail - hydrophilic head}-{hydrophilic head-hydrophobic tail} – configuration (figure 4).
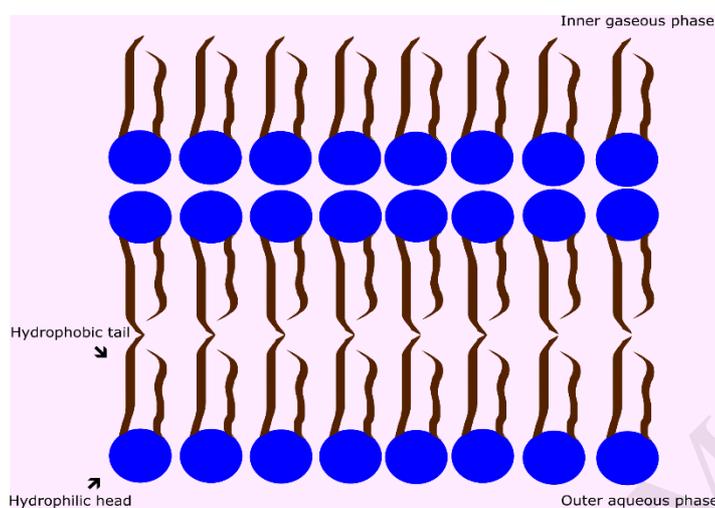

Figure 4. cartoon highlighting the trilayer structure of our phospholipid-shelled MBs

We are reporting to the best of our knowledge, under the context of phospholipid MB-shell, an accurate thickness value for our MBs and present a novel method for quantifying this parameter prior to AFM force-curve analysis. Thus, it is this value which we used in the following mathematical theories when analysing the mechanical properties of the MBs, as opposed to the conjectural values used before. Furthermore, factors that could cause variation in the true thickness value of MB shell membranes, such as the types of lipid used should always be taken into account - and so we highlight this type of investigation should be conducted for each different MB formulation that is used in order to accurately depict the thickness value. Furthermore, the tri-layer structure is compatible with the MB asymmetry in surface energy: hydrophobic interior (gas) and hydrophilic exterior (water). Our experiments indicate strongly that the actual configuration is a trilayer and not a monolayer.

Mechanical Characterisation

Microbubble Compression

The typical force-deformation (F-Δ) curve shown (figure 5a) was obtained through force-curve mode using AFM. During approach, there is no deflection of the cantilever prior to coming into physical contact with the bubble. As the cantilever gets even closer, in the nanometre scale, there are van der Waal's forces, as well as polar/ionic forces which begin to affect the force signal. Once contact is made, there is cantilever deflection upwards due to the repulsive force from the MB (the initial part of which originates from the PEG layer), until a maximum is reached, around 90 nN (figure 5a). During this contact phase, the cantilever is compressing the sample. The next phase is the retract phase, at the point where the MB has been compressed to its maximum,

the cantilever is then retracted. During withdrawal and before detachment; adhesive interactions occur between cantilever and sample, these are non-specific and can be visualised through the inflections, and cause a local minimum force in the deflection of the cantilever. As the cantilever is continually pulled from the MB there are further stretching interactions until eventually the cantilever undergoes a process known as 'snapping off'. At this stage, the cantilever breaks free and returns to its starting position.
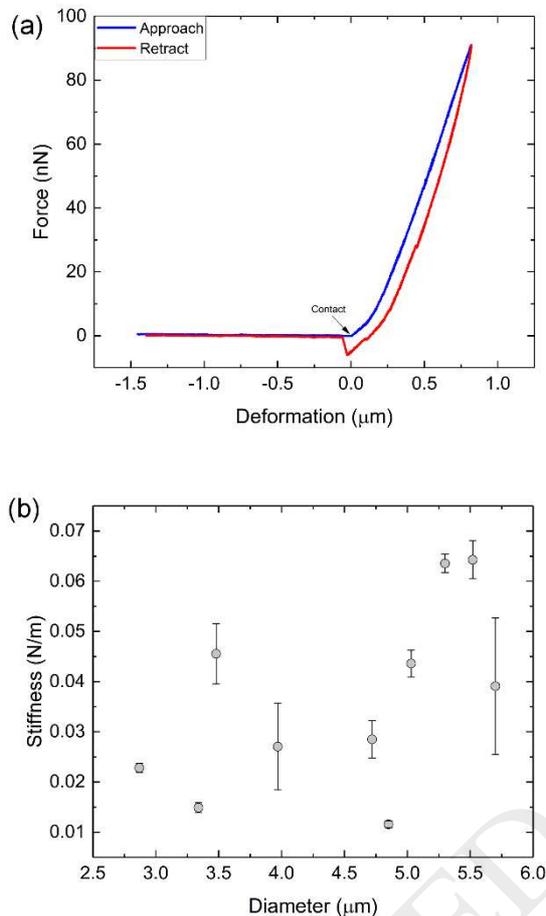

Figure 5. (a) Typical Force-Deformation curve acquired on a MB with diameter of 3.48 μm. Blue curve represents approach and contact stages, red curve represents retraction of the cantilever from the MB. Hysteresis between loading and unloading can be attributed to the viscoleastic properties of the MB (the inherent non-linearity/hysteresis of the piezoelectric relationship between movement and applied voltage is limited due to the closed-loop piezo of the MFP-1D). (b) MB stiffness as a function of diameter (μm) for ten MBs, which is derived from the linear gradient of the F-Δ curves.

Stiffness

The stiffness values (figure 5b) of 10 MBs with diameters ranging from 2.87 µm to 5.7 µm were calculated by taking the gradient of the F-Δ curves from the linear region of the curve (ignoring the initial non-linear region). Compressing a MB with a cantilever, similarly to what has been done in this investigation, can be modelled as two springs in a series (47). When calculating the force applied to the MB by using Hooke's Law (equation 1), one can determine the stiffness, (k_b) by taking the gradient of the F-Δ curve as it gives the MB stiffness at any given force.

Ten curves were analysed from each MB, which yielded spring constant values ranging from a minimum of 0.01 ± 0.001 N/m to a maximum of 0.064 ± 0.003 N/m. The mean values of our data show a general trend that as MB diameter increases, so too does the YM value, highlighting the reproducibility of our MBs. Similar scatters have been seen before when using AFM to characterise spherical capsules, and like the present study,

showed no sign of any plastic deformation when repeating the compression numerous times to a maximum force of 120 nN (48).

The distribution of the obtained stiffness values (figure 5b) display a trend that as MB diameter increases, the stiffness value also increases. Previous work by Chen et al (49) using similar methodology on MBs composed of DSPC: DSPE-PEG$_{2000}$: DSPE-PEG$_{2000}$-C at a molar ratio of 90:5:5; showed shell spring constants of 0.004 N/m to a maximum of 0.024 N/m for MBs ranging from 4-8 μm, demonstrating that our in-house MBs are much stiffer across a comparative diameter range, despite similar shell formulation. Our MBs were produced using a T-junction microfluidic device compared with the sonication method used by Chen et al (49). Previous work has shown the advantages that come with this newer manufacturing method. Due to the specific microchannel and microintegral components which is coupled with specific geometries, T-junction microfluidic devices can provide highly accurate monodisperse samples with uniform shell thickness and composition. Whereas a downfall with sonication is that it creates uncontrolled shear that can result in MBs with differing shell thickness, a factor which could also account for the stiffer MBs seen in the present study (50).

Earlier AFM work assessing stiffness values has shown mixed results when trying to establish a general relationship between MB diameter and MB stiffness; with some studies showing an exponential decay relationship between stiffness and MB-diameter, such as the findings from McKendry et al and Chen et al (49,51). However, we have not shown such a decay relationship in the present study or with previous work which used different phospholipid MBs (29). To address this difference in results it is important to consider the shell at the molecular level. Kwan and Borden (52) state that at diameters less than ~ 6 μm, the lipid molecules in the shell become 'jammed', consequently increasing the MB spring constant. If this is the case then an inverse correlation should always be seen with these investigations. As this is not the case, there must be other factors interfering. And so the membrane domain formation is of interest; phospholipids can organise in domains with order and/or disorder (53); the competition between these domains and the structural defects at their boundaries could vary from system to system and generate varied responses (54).

Young's Modulus

To truly understand these MBs, which are colloidal systems consisting of lipid-stabilised gas bubbles suspended in an aqueous medium that can resonate at ultrasonic frequencies, it is important to address the physico-chemical properties of the MB shell as this is the key structural element which strongly dictates the quality of the acoustic response. When sonicating with high mechanical index values during ultrasound imaging, the MBs absorb the acoustic energy and begin to oscillate – causing violent expansion and contraction of the bubble (55). Eventually the molecular area of the shell membrane reaches a critical value where it cannot be compressed or expanded any further. It is at this state where any further forces result in fracturing / buckling of the shell membrane (56). Nevertheless, this is the phenomenon which significantly improves contrast during ultrasonic imaging. Phospholipid-shelled MBs have shown favourable contrast enhancement in high frequency ultrasound imaging (57). Thus, it is imperative that the correct models are used to evaluate the elasticity of the shell membrane. For most simple elastic materials, the Young's Modulus can be determined from the gradient of the stress-strain curve within the linear elastic region when a force is applied (58). For MBs, the geometry is complicated and therefore more detailed mechanical models have to be used. We have employed both the Reissner and Hertz contact models in an attempt to quantify Young's Modulus and offer an assessment as to what model is more suited for use in data generated from AFM-MB investigations. These measurements using the AFM not only provide information on the Young's Modulus of individual MBs but also how Young's Modulus changes as the diameter of the MBs change.

Reissner Theory

Understanding the elastic mechanics of a spherical shell has been of interest since the first fundamental results produced in 1912 (59). Today the Reissner theory can be applied to phospholipid MBs as a linear

theory which, originally designed for shallow spherical caps undergoing point-like loads, can be applied to structures undergoing non-point like loads over a slightly larger contact area (7,59,60). This analytical theory has been used before on polymeric MBs (61) as well as phospholipid vesicles (62). In order to derive Young's Modulus values that allow for comparison between MBs of different sizes, we had to define a dimensionless parameter - relative deformation, which is denoted as, ε. It is defined as $\varepsilon=\frac{MB\ Deformation}{D}$, where D is the diameter of the MB. We have fitted regions of relative deformation up to around $\varepsilon = 0.1$ to satisfy the requirement of the model (small deformations). The Young's Modulus, (E), could then be calculated using the thickness of the MB-shell (t), 6.3 nm – this is the value which we quantified through the tapping mode investigations (figures 2 and 3), using the following equation [29].

$$E = \frac{2\sqrt{3}(1-v^2)}{8t^2}\ \frac{F}{\varepsilon} \qquad\qquad (2)$$

Where, Poisson's ratio (v), is taken as 0.5 for soft-shelled MBs [29]; F is the applied force taken from the force-curve (note that the factor 2 in the numerator arises from the fact that the original theory considered the deformation of a fixed arc and not a whole sphere that will be deformed in both poles; this factor has been neglected in earlier work).
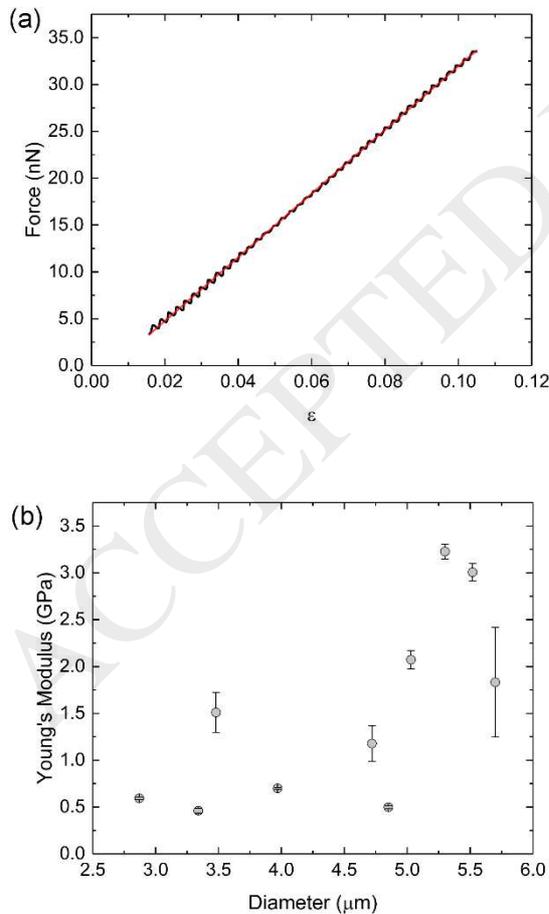
*Figure 6. (a) A typical linear part of a F − ε curve. The red line shows the linear fit and its gradient is used in equation 3. This curve is from a MB with D = 5.53 µm. (b) Elasticity values representative of the shells of 10 different MBs, all calculated using the Reissner model.*

Data from 10 MBs (minimum 30 curves per bubble) was taken from ε = 0.01 ± 0.02 to a maximum of ε = 0.14 ± 0.02. Figure 6a shows a typical linear region of an F-ε curve. Taking these values and applying them to the Reissner model yielded mean Young's Moduli ranging from 0.23 ± 0.01 GPa to 1.61 ± 0.04 GPa (figure 6b). The calculated values from our investigation coincide with other phospholipid MBs with similar material assemblies, which also showed bubble elasticity in the GPa region (30,33) when evaluated with this theory.

When comparing results from the Reissner theory on soft-shelled MBs it becomes apparent that the Reissner theory yields values that are an order of magnitude higher than expected for phospholipid systems from previous work (30,63). Previous calculations based on membrane theory looking at soft-shelled FDA approved Definity MBs gave values in the region of 8-38 MPa [29]. Although 10μl of perfluorohexane is added in our MB solution and it has been shown previously to cause a slight decrease in elasticity (36). It is worthwhile noting that the parameter accounting for shell thickness, (t), is what has a significant impact on the overall outcome when using Reissner Theory. Previous studies assumed thickness of 2.5 nm, producing YM values within the GPa region (30). However, if we were to assume thickness of >10 nm, our values drop an order of magnitude into the 100 MPa range. Through our tapping mode investigations, we have quantified our shell thickness to be 6.3 nm and have then proceeded to use this value when analysing our force-curve data.

Thus, we conclude for the first time with certainty that although Reissner equation can produce E values which are reasonable for polymeric MBs (61), it can overestimate E values for soft-shelled MBs. As a result, it is therefore not a suitable model in this context.

Hertz Theory

Hertz' contact problem is a well-known classical problem in elastic mechanics. Originally derived to determine elasticity of two homogenous spheres in contact, modifications in the theory over the last 100 years have allowed for the assessment of more complex contact problems. With the ability to now illustrate the elastic deformation of two completely different geometries touching under load, we could employ this theory for our plate-sphere compressions, assuming we treated the MB as a homogenous sphere (64,65). Doing so meant that any E values produced had to be interpreted with the assumption that the MBs were modelled as homogenous microspheres, and not a gas-filled bubble with a shell, as we described using the Reissner approximation.

The model proposes that any deformation occurs locally, with the rest of the 'sphere' upholding its structural integrity. Lulevich et al., who studied cell mechanics of live and dead cells using AFM (25), used Hertz theory to determine the relationship between force and deformation using tipless cantilevers as:

$$F = \frac{\sqrt{2}\,E}{3\,(1-v^2)}\,R_0^{\,2}\,\varepsilon^{1.5} \qquad (3)$$

Where F is the applied force, R_0 is MB radius, v is Poisson's ratio and ε is relative deformation. Again, this model accounts for small linear deformations. We have taken ε of 0.6 for each curve analysed to satisfy requirements of the model. By taking the gradient of the F-$\varepsilon^{1.5}$ curve, we could derive E by rearranging equation 3 to:

$$E = \frac{3\,(1-v^2)}{\sqrt{2}\,R_0^{\,2}}\,\frac{F}{\varepsilon^{1.5}} \qquad (4)$$
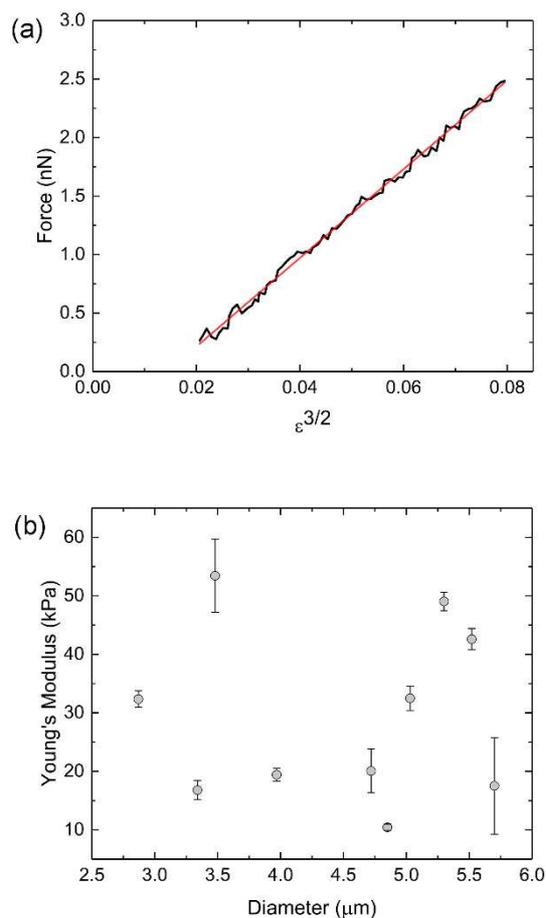
Figure 7. Linear region of a $F - \varepsilon^{1.5}$ curve taken from a MB with diameter of 2.87 μm. The dashed line represents the linear fit, with the gradient taken for the equation to determine the elasticity. (b) Young's Modulus values for ten microbubbles with different diameters, all calculated using the Hertz model.

Figure 7a represents a typical F-$\varepsilon^{1.5}$ curve. We show data on 10 bubbles with values ranging from 10.4 ± 0.1 kPa to 53.4 ± 6.2 KPa (figure 7b). Interestingly, treating MBs as homogenous microspheres produced Young's Modulus values two orders of magnitude lower than when the shell was evaluated using the Reissner model. The data in the $10.4 - 53.4$ kPa range is significantly lower than previous studies conducted on phospholipid MBs which displayed values of 93 to 233 kPa. Although both sets of MBs were soft-shelled, there was a difference in lipid composition that could be a factor which caused such a difference between the two studies (29). As we know that perfluorohexane is present in our shell membrane and has previously been shown to decrease elasticity (36); thus, it could be a reason for why our values were lower. Furthermore, the present study, and the one aforementioned, compressed the MB in the same manner, the loading variable can be excluded as a contributing factor when discussing the variation seen amongst the data sets. Evidence from Sboros et al. confirms this it was reported that small differences in the scanning rate produced no significant effects on the MB (47).

Nevertheless, the main benefit from analysing in this manner comes from the ability to draw comparisons to those from biological studies looking at cell mechanics. Hertz is a widely used analysis technique in the biological setting. It has been shown that this model is applicable to mechanical research on cells (66) . In cells, the local deformation results from the intracellular polymeric network of different proteins such that the cell has varying mechanical properties at different locations (66). Investigations on endothelial cells using this model yielded E values of 1.4 ± 0.1 to 6.8 ± 0.4 kPa, with cardiac cells showing higher E values up to 100.3 ± 10.7 kPa. Platelets, which play a role in inflammatory response and have a different shape to other cells

within the vasculature, yielded E values in the region of 1-50 kPa (67). Regardless of shape (and size), which is a consequence of the internal polymeric cytoskeletal structure, cells within the vasculature show Young's Modulus values within the same kPa region as our in-house MBs. Shown here is a brief overview of other machineries in-vivo that MBs will come in to contact with. We conclude that the Hertz model is a valuable tool when evaluating YM as direct comparisons can be made to other structures which follow similar deformation regimes as the MBs.

PEG-Brush Thickness

The physico-chemical characterisation of the PEG chains which are end-grafted to our lipids is important for not only polymer physics but has biological significance as well (68). In our AFM experiments we were able to detect the cantilever compressing the PEG brush layer. This was made possible by our decision to use tipless cantilevers, as a sharp tipped-cantilever could easily pass through the brush without necessarily detecting any repulsive force. Secondly, the tipless cantilevers went on to compress the MBs and it was the nanoscale interrogation of the force-curves which allowed for this detection. During the approach phase of the force-curve, we observed a gradual non-linear repulsive force as the cantilever approached the shell of the MB. Due to the lack of adhesion at this point, coupled with the observation of the non-linear repulsive force, we concluded that we were in fact compressing the PEG brush; as its behaviour in this set up was comparable with its ability to how it prevents aggregation of colloidal particles. To analyse this data an appropriate brush quantification theory had to be employed. There have been several theoretical approaches to calculate the compressive force between polymer-brush layers (69,70). We opted for the Alexander de Gennes theory (71) as it is based on simple scaling arguments and it is conceptually easier to implement in our geometry.

When measuring forces between surfaces having fixed geometry, it is in fact experimentally better to use curved surfaces than two flat surfaces, and is the reason that most measurements are conducted between a sphere and a flat surface, two spheres or crossed cylinders (72). We have exploited the relationship derived from the Derjaguin approximation that expresses the force profile acting between two bodies. It is commonly used for colloidal particles as it expresses the force between two bodies as a function of its separation (73). At the start of the experiment, $F(Z)$ will be 0 as the cantilever is far away from the MB; as the force-measuring cantilever is moved by a known amount to a new position, the surface separation changes and a force profile is recorded. This allows us to determine a relationship for PEG compression. By applying the Derjaguin Approximation to the Alexander de Gennes theory of a polymer brush (71), the following relationship can be derived;

$$F\,(Z) \sim \exp\left(\frac{-2\pi Z}{L_0}\right) \qquad\qquad (5)$$

Whereby $F(Z)$ is the force exerted on the cantilever by the brush at separation (Z) between the probe surface and solid substrate and L_0 is the brush thickness (74).

The inclusion of PEG within our MB shell membrane means that these end-grafted polymer chains protrude from the shell membrane, overlap one another and stretch away from the shell membrane producing a brush layer (33,75). As our tipless cantilever compresses the brush layer we expect that the chains would resist the applied force in the manner of a non-linear spring resisting compression, as seen by Stan et al. (76). Stan and colleagues showed, using AFM, that as a PEG brush layer is compressed it resists compression non-linearly through polymer chain entropic interactions. Through the analysis of our own AFM F-Δ curves (in this regime $Z=\Delta$) we discovered that we were in fact probing these properties at the nano level for our system.
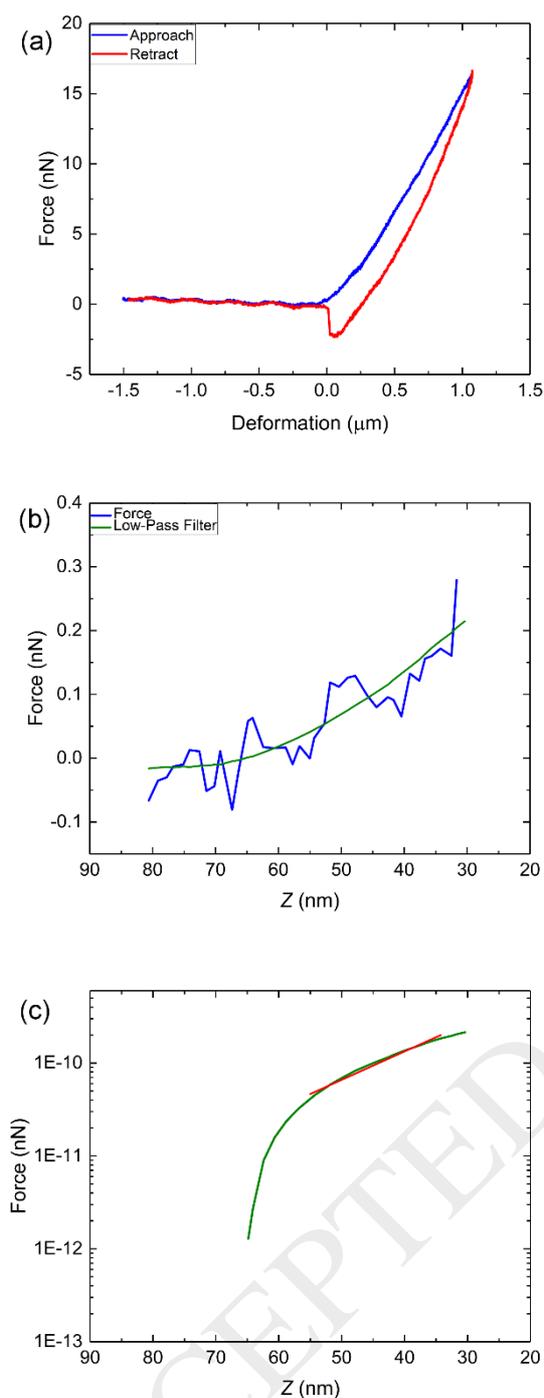
Figure 8. (a) A raw F-Δ curve acquired on MB with diameter of 3.34 μm (b) F-Z curve showing the PEG region as the cantilever moves through prior to making contact with the shell. (c) F-Z curve in semi-logarithmic scale to proceed with analysis using Alexander-De Gennes theory of a polymer brush.

Figure 8a represents a typical Force-deformation curve obtained through force-curve mode using AFM. Figure 8b highlights the PEG region with low-pass filtering (green) to account for the background noise. Figure 8c shows the transformation of the curve of the PEG region to semi-logarithmic scale so we could proceed with analysis using the Alexander-De Gennes theory. We discovered that during the approach phase, and within a region of some of tens of nm prior to the cantilever meeting the MB, a non-linear resistance could be observed, which is related to the PEG brush. The lack of adhesion between tip and sample at this stage indicates that there is steric repulsion, demonstrating that the brush layer is behaving in our experiments as one would desire it to behave when moving freely in solution and in-vivo. The evidence for the presence of this brush layer

protruding from our MBs builds upon the work of Abou-Saleh et al (33). PEG conformation can be identified when taking certain factors into account. The controlling factor is the distance (D) between the PEG chains in the lipid membrane relative to the Flory dimension, R_F. Through calculating R_F, which is $R_F = aN^{\frac{3}{5}}$, whereby a is the monomer size and N is the number of units in the polymer, one can deduce the configuration. When $D > 2R_F$ there is a mushroom configuration – the chains form a typical random coil that mimics a mushroom shape. And when $D < 2R_F$, the system is at the brush regime (77). Using these calculations, Abou-Saleh et al(33) showed at $\geq$ 5% molar concentration in a MB membrane formulation (akin to ours), the PEG layer constitutes a brush configuration. We use a 5% DSPE-PEG$_{2000}$ molar ratio in our formulation and thus a polymer brush analysis is justified.

We show data on 7 MBs (figure 9) with brush thickness (L_0) values ranging from 83 nm to 230 nm (figure 9). We again show a trend that as diameter of a MB increases, so does the mechanical / nanostructural parameter tested. We stress that these values are not to be taken as the literal brush thickness as factors such as positioning of polymer islands and solvent conditions including ionic forces can affect the overall interaction region. Furthermore, contrary to classical brush systems where the brush is grafted in a solid surface, in our system the brush is grafted on a soft-shelled hollow sphere. It is conceivable that we compress, at the same time, the compliant shell as well, especially as the compression progresses, encompassing a higher area of contact. Nonetheless, it appears, generally, that at larger MB diameter, we have a larger L_0 value. This trend could be suggestive that as diameter increases, there is greater grafting densities within the shell, which will in turn result in a more extended brush regime.
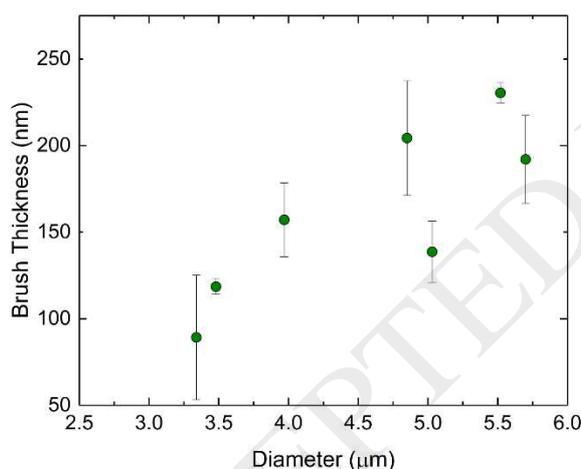

Figure 9. L_0 values for seven MBs with different diameters, calculated using Alexander-De Gennes Theory. Data is indicative that as diameter increases, so too does the PEG brush thickness.

Through our ability to probe the nanostructural PEG-brush using AFM, we observed another interesting phenomenon by which not all our MBs displayed this initial non-linear resistance upon compression. This indicates that PEG distribution, density and thickness may not be as homogenously distributed as previously thought. For MBs to be used as effective contrast agents, the uniformity of the PEG layer is imperative to protect the shell surface – which directly impacts survival, biocompatibility and resistance to coalescence in-vivo (78). Through this observed phenomenon, we find that we agree with previous work from Tanwir and Tsoukanova (79). They visualised through epifluorescence microscopy that there is non-ideal mixing of PEGylated phospholipids with other phospholipids.

Through nano-interpretation of our F-Δ curves we have shown that the Alexander-De Gennes theory of a polymer brush can be applied to gain insight in to the thickness of the brush layer. Through this we have also

identified PEG mixing in the phospholipid matrix may not be ideal, opening avenues for further quantification to proceed. It is vital PEG properties are quantified if MBs are to become part of routine health care.

Conclusions

In this study, we have exploited the potential of atomic force microscopy in characterising the mechanical and nanostructural properties of our in-house phospholipid microbubbles. Using tapping mode imaging we have quantified with a high level of accuracy the thickness of phospholipid shells (6.3 nm indicating a trilayer structure), a parameter which is extremely useful in MB design and development, both in future simulations and experimental work. To the best of our knowledge, this is the first time this parameter has been directly measured in relation to microbubbles. Furthermore, we have demonstrated the impact that this value can have on force-curve investigations when reporting Young's Modulus using the Reissner theory. We have shown that slight variations in the shell thickness value, even just a few nanometres, can significantly misrepresent the Young's Modulus value by an order of magnitude. Using for the first time the measured (by AFM imaging) shell thickness value, we showed that Reissner theory is not suitable for the prediction of the elastic properties of soft-shelled MBs.

Our force measurements allowed us to also observe the non-linear compressions within the nm region prior to the contact phase, which we believe is related to the force originating from the PEG layer as it is resisting compression from the cantilever. We then employed Alexander – De Gennes theory of a polymer brush to provide information regarding the thickness of this brush, a vital component in MB design as it enables the bubbles to elude immunogenic detection in-vivo. We suggest that one should also take into account the softness of the shell, which can be simultaneously compressed, to interpret the overestimated thickness values. We also found that this non-linear resistance to deformation presented significant variability, opening avenues for future research to establish and further quantify whether the PEG layer is as homogenously distributed throughout the shell as it is currently believed to be.

Through combining the complex force measurements with tapping-mode imaging we were able to explore the various mechanical and nanostructural properties of our system. Exploiting these unique characterisation capabilities of the AFM will impact not only the development of a novel theranostic agent, but also formulate and provide an in-sight on how to specifically design, develop and understand a targeting agent in the future on a much wider scale.

Acknowledgements

References

1.   Wilson SR, Greenbaum LD, Goldberg BB. Contrast-enhanced ultrasound: What is the evidence and what are the obstacles? American Journal of Roentgenology. 2009. p. 55–60.
2.   Kulak O, Guner GH, Supciller AA. A new multi criteria decision making approach for medical imaging systems considering risk factors. Appl Soft Comput. Elsevier; 2015 Oct 1;35:931–41.

3. Hoskins PR. Haemodynamics and blood flow measured using ultrasound imaging. Proc Inst Mech Eng Part H J Eng Med. 2010;224(2):255–71.

4. Hernot S, Klibanov AL. Microbubbles in ultrasound-triggered drug and gene delivery. Adv Drug Deliv Rev. 2008;60(10):1153–66.

5. Moran C, Ross J a., Cunningham C, Butler M, Anderson T, Newby D, et al. Manufacture and acoustical characterisation of a high-frequency contrast agent for targeting applications. Ultrasound Med Biol. 2006;32(3):421–8.

6. McLaughlan JR, Harput S, Abou-Saleh RH, Peyman SA, Evans S, Freear S. Characterisation of Liposome-Loaded Microbubble Populations for Subharmonic Imaging. Ultrasound Med Biol. Elsevier; 2017 Jan 1;43(1):346–56.

7. Dieluweit S, Csiszár A, Rubner W, Fleischhauer J, Houben S, Merkel R. Mechanical Properties of Bare and Protein-Coated Giant Unilamellar Phospholipid Vesicles. A Comparative Study of Micropipet Aspiration and Atomic Force Microscopy. Langmuir. American Chemical Society; 2010 Jul 6;26(13):11041–9.

8. Sidorov AR, Zhang Y, Grigorenko AN, Dickinson MR. Nanometric laser trapping of microbubbles based on nanostructured substrates. Opt Commun. 2007;278(2):439–44.

9. Ibsen S, Schutt CE, Esener S. Microbubble-mediated ultrasound therapy: A review of its potential in cancer treatment. Drug Design, Development and Therapy. 2013. p. 375–88.

10. Kiessling F, Gaetjens J, Palmowski M. Application of Molecular Ultrasound for Imaging Integrin Expression. Theranostics. 2011;1(1):127–34.

11. Xiong X, Zhao F, Shi M, Yang H, Liu Y. Polymeric Microbubbles for Ultrasonic Molecular Imaging and Targeted Therapeutics. J Biomater Sci Polym Ed. 2011 Jan;22(4–6):417–28.

12. Searle J, Mendelson R, Zelesco M, Sanford J, Cheng W, McKinstry C, et al. Non-invasive prediction of the degree of liver fibrosis in patients with hepatitis C using an ultrasound contrast agent. A pilot study. J Med Imaging Radiat Oncol. Blackwell Publishing Asia; 2008 Apr 1;52(2):130–3.

13. Lum AFH, Borden MA, Dayton PA, Kruse DE, Simon SI, Ferrara KW. Ultrasound radiation force enables targeted deposition of model drug carriers loaded on microbubbles. J Control Release. 2006;111(1–2):128–34.

14. Sboros V, Glynos E, Ross J a, Moran CM, Pye SD, Butler M, et al. Probing microbubble targeting with atomic force microscopy. Colloids Surf B Biointerfaces. 2010;80(1):12–7.

15. Mico V, Charalambous A, Peyman SA, Abou-Saleh RH, Markham AF, Coletta PL, et al. Evaluation of lipid-stabilised tripropionin nanodroplets as a delivery route for combretastatin A4. Int J Pharm. Elsevier; 2017 Jun 30;526(1–2):547–55.

16. Lozano MM, Longo ML. Microbubbles coated with disaturated lipids and DSPE-PEG2000: Phase behavior, collapse transitions, and permeability. Langmuir. American Chemical Society; 2009 Mar 17;25(6):3705–12.

17. de Jong N, Bouakaz A, Frinking P. Basic Acoustic Properties of Microbubbles. Echocardiography. Blackwell Futura Publishing, Inc.; 2002 Apr 1;19(3):229–40.

18. Kollmann C. New sonographic techniques for harmonic imaging-Underlying physical principles. European Journal of Radiology. 2007. p. 164–72.

19. Wallace N, Wrenn SP. Ultrasound triggered drug delivery with liposomal nested microbubbles. Ultrasonics. Elsevier; 2015 Dec 1;63:31–8.

20. Kenwright DA, Anderson T, Moran CM, Hoskins PR. Assessment of Spectral Doppler for an Array-Based Preclinical Ultrasound Scanner Using a Rotating Phantom. Ultrasound Med Biol. Elsevier; 2015 Aug;41(8):2232–9.

21. Binnig G, Quate CF. Atomic Force Microscope. Phys Rev Lett. 1986;56(9):930–3.

22. Guo G, Tu J, Guo X, Huang P, Wu J, Zhang D. Characterization of mechanical properties of hybrid contrast agents by combining atomic force microscopy with acoustic/optic assessments. J Biomech. Elsevier; 2016 Feb 8;49(3):319–25.

23. Borin D, Pecorari I, Pena B, Sbaizero O. Novel insights into cardiomyocytes provided by atomic force microscopy. Seminars in Cell and Developmental Biology. Academic Press; 2018. p. 4–12.

24. Yeow N, Tabor RF, Garnier G. Atomic force microscopy: From red blood cells to

immunohaematology. Advances in Colloid and Interface Science. Elsevier; 2017. p. 149–62.

25. Lulevich V, Zink T, Chen HY, Liu FT, Liu GY. Cell mechanics using atomic force microscopy-based single-cell compression. Langmuir. American Chemical Society; 2006;22(19):8151–5.

26. Birukova AA, Arce FT, Moldobaeva N, Dudek SM, Garcia JGN, Lal R, et al. Endothelial permeability is controlled by spatially defined cytoskeletal mechanics: atomic force microscopy force mapping of pulmonary endothelial monolayer. Nanomedicine. 2009 Mar;5(1):30–41.

27. de Pablo PJ. Atomic force microscopy of virus shells. Seminars in Cell and Developmental Biology. Academic Press; 2018. p. 199–208.

28. Cappella B, Dietler G. Force-distance curves by atomic force microscopy. Surf Sci Rep. 1999;34(1–3):1–104.

29. Buchner Santos E, Morris JK, Glynos E, Sboros V, Koutsos V. Nanomechanical properties of phospholipid microbubbles. Langmuir. 2012;28(13):5753–60.

30. Abou-Saleh RH, Peyman SA, Critchley K, Evans SD, Thomson NH. Nanomechanics of lipid encapsulated microbubbles with functional coatings. Langmuir. American Chemical Society; 2013 Mar 26;29(12):4096–103.

31. Heath GR, Abou-Saleh RH, Peyman SA, Johnson BRG, Connell SD, Evans SD. Self-assembly of actin scaffolds on lipid microbubbles. Soft Matter. 2014;10(5):694–700.

32. Ferrara KW, Borden MA, Zhang H. Lipid-Shelled Vehicles: Engineering for Ultrasound Molecular Imaging and Drug Delivery. Acc Chem Res. 2009;42(7):881–92.

33. Abou-Saleh RH, Swain M, Evans SD, Thomson NH. Poly(ethylene glycol) lipid-shelled microbubbles: Abundance, stability, and mechanical properties. Langmuir. American Chemical Society; 2014 May 20;30(19):5557–63.

34. Peyman SA, McLaughlan JR, Abou-Saleh RH, Marston G, Johnson BRG, Freear S, et al. On-chip preparation of nanoscale contrast agents towards high-resolution ultrasound imaging. Lab Chip. 2016;16(4):679–87.

35. Dhanaliwala AH, Chen JL, Wang S, Hossack JA. Liquid flooded flow-focusing microfluidic device for in situ generation of monodisperse microbubbles. Microfluid Nanofluidics. 2013;14(3–4):457–67.

36. Abou-Saleh RH, Peyman SA, Johnson BRG, Marston G, Ingram N, Bushby R, et al. The influence of intercalating perfluorohexane into lipid shells on nano and microbubble stability. Soft Matter. 2016;12(34):7223–30.

37. Peyman SA, Abou-Saleh RH, Evans SD. 3D expanding geometry. US9802165B2, 2011.

38. Miranda PB, Xu L, Shen YR, Salmeron M. Icelike water monolayer adsorbed on mica at room temperature. Phys Rev Lett. 1998;81(26):5876–9.

39. Nečas D, Klapetek P. Gwyddion: an open-source software for SPM data analysis. Open Phys. SP Versita; 2012 Jan 1;10(1):181–8.

40. Lévy R, Maaloum M. Measuring the spring constant of atomic force microscope cantilevers: thermal fluctuations and other methods. Nanotechnology. IOP Publishing; 2002 Feb 1;13(1):33–7.

41. Lewis BA, Engelman DM. Lipid bilayer thickness varies linearly with acyl chain length in fluid phosphatidylcholine vesicles. Journal of Molecular Biology. Academic Press; 1983. p. 211–7.

42. Nagle JF, Tristram-Nagle S. Structure of lipid bilayers. Biochimica et Biophysica Acta - Reviews on Biomembranes. NIH Public Access; 2000. p. 159–95.

43. Mashaghi A, Partovi-Azar P, Jadidi T, Nafari N, Maass P, Tabar MRR, et al. Hydration strongly affects the molecular and electronic structure of membrane phospholipids. J Chem Phys. American Institute of Physics; 2012 Mar 21;136(11):114709.

44. Kučerka N, Tristram-Nagle S, Nagle JF. Closer Look at Structure of Fully Hydrated Fluid Phase DPPC Bilayers. Biophys J. The Biophysical Society; 2006 Jun 1;90(11):L83–5.

45. Unsay JD, Cosentino K, García-Sáez AJ. Atomic Force Microscopy Imaging and Force Spectroscopy of Supported Lipid Bilayers. J Vis Exp. MyJoVE Corporation; 2015 Jul 22;(101):e52867.

46. Kwan JJ, Borden MA. Lipid monolayer collapse and microbubble stability. Adv Colloid Interface Sci. Elsevier; 2012 Nov 15;183–184:82–99.

47. Sboros V, Glynos E, Pye SD, Moran CM, Butler M, Ross J, et al. Nanointerrogation of ultrasonic contrast agent microbubbles using atomic force microscopy. Ultrasound Med Biol. 2006;32(4):579–

85.

48. Elsner N, Dubreuil F, Weinkamer R, Wasicek M, Fischer FD, Fery A. Mechanical properties of freestanding polyelectrolyte capsules: A quantitative approach based on shell theory. Prog Colloid Polym Sci. Berlin/Heidelberg: Springer-Verlag; 2006;132:117–23.

49. Chen CC, Wu SY, Finan J, Morrison B, Konofagou E. An experimental study on the stiffness of size-isolated microbubbles using atomic force microscopy. IEEE Trans Ultrason Ferroelectr Freq Control. NIH Public Access; 2013 Mar;60(3):524–34.

50. Lin H, Chen J, Chen C. A novel technology: microfluidic devices for microbubble ultrasound contrast agent generation. Medical and Biological Engineering and Computing. Springer Berlin Heidelberg; 2016. p. 1317–30.

51. McKendry JE, Grant CA, Johnson BRG, Coletta PL, Evans J a., Evans SD. Force spectroscopy of streptavidin conjugated lipid coated microbubbles. Bubble Sci Eng Technol. 2010 May;2(2):48–54.

52. Kwan JJ, Borden MA. Microbubble dissolution in a multigas environment. Langmuir. American Chemical Society; 2010 May 4;26(9):6542–8.

53. Kaiser H-J, Lingwood D, Levental I, Sampaio JL, Kalvodova L, Rajendran L, et al. Order of lipid phases in model and plasma membranes. Proc Natl Acad Sci. PNAS; 2009;106(39):16645–50.

54. Belička M, Weitzer A, Pabst G. High-resolution structure of coexisting nanoscopic and microscopic lipid domains. Soft Matter. The Royal Society of Chemistry; 2017 Mar 1;13(9):1823–33.

55. Domenici F, Brasili F, Oddo L, Cerroni B, Bedini A, Bordi F, et al. Long-term physical evolution of an elastomeric ultrasound contrast microbubble. J Colloid Interface Sci. Academic Press; 2019 Mar 22;540:185–96.

56. Helfield B. A Review of Phospholipid Encapsulated Ultrasound Contrast Agent Microbubble Physics? Ultrasound in Medicine and Biology. Elsevier; 2018 Feb 1;282–300.

57. Sun C, Sboros V, Butler MB, Moran CM. InVitro Acoustic Characterization of Three Phospholipid Ultrasound Contrast Agents from 12 to 43 MHz. Ultrasound Med Biol. Elsevier; 2014 Mar 1;40(3):541–50.

58. Lee C, Wei X, Kysar JW, Hone J. Measurement of the Elastic Properties and Intrinsic Strength of Monolayer Graphene. Science (80-). American Association for the Advancement of Science; 2008 Jul 18;321(5887):385–8.

59. Reissner E. Stresses and Displacements of Shallow Spherical Shells. J Math Phys. 1946 Apr;25(3):279–300.

60. Reissner E. Stresses and small displacements of shallow spherical shells. II. J Math Phys. 1946 Apr;25(1–4):80–5.

61. Glynos E, Koutsos V, McDicken WN, Moran CM, Pye SD, Ross JA, et al. Nanomechanics of biocompatible hollow thin-shell polymer microspheres. Langmuir. 2009;25(13):7514–22.

62. Schäfer E, Vache M, Kliesch T-T, Janshoff A. Mechanical response of adherent giant liposomes to indentation with a conical AFM-tip. Soft Matter. 2015;11:4487–95.

63. Cavalieri F, Best JP, Perez C, Tu J, Caruso F, Matula TJ, et al. Mechanical Characterization of Ultrasonically Synthesized Microbubble Shells by Flow Cytometry and AFM. ACS Appl Mater Interfaces. American Chemical Society; 2013 Nov 13;5(21):10920–5.

64. Tian-quan Y. The exact integral equation of Hertz's contact problem. Appl Math Mech. 1991 Feb;12(2):181–5.

65. Radmacher M, Fritz M, Kacher CM, Cleveland JP, Hansma PK. Measuring the viscoelastic properties of human platelets with the atomic force microscope. Biophys J. 1996;70(1):556–67.

66. Mahaffy RE, Shih CK, MacKintosh FC, Käs J. Scanning probe-based frequency-dependent microrheology of polymer gels and biological cells. Phys Rev Lett. 2000;85(4):880–3.

67. Mathur AB, Collinsworth AM, Reichert WM, Kraus WE, Truskey GA. Endothelial, cardiac muscle and skeletal muscle exhibit different viscous and elastic properties as determined by atomic force microscopy. J Biomech. Elsevier; 2001 Dec 1;34(12):1545–53.

68. Hansen PL, Cohen JA, Podgornik R, Parsegian VA. Osmotic properties of poly(ethylene glycols): Quantitative features of brush and bulk scaling laws. Biophys J. 2003;84(1):350–5.

69. Milner ST, Witten TA, Cates ME. Theory of the Grafted Polymer Brush. Macromolecules. American

Chemical Society; 1988 Aug;21(8):2610–9.

70. Kreer T. Polymer-brush lubrication: A review of recent theoretical advances. Soft Matter. Royal Society of Chemistry; 2016. p. 3479–501.

71. de Gennes PG. Polymers at an interface; a simplified view. Advances in Colloid and Interface Science. 1987. p. 189–209.

72. Israelachvili JN. Intermolecular and Surface Forces. In: Intermolecular and Surface Forces. 2011. p. 1–30.

73. Derjaguin B. Untersuchungen über die Reibung und Adhäsion, IV. Kolloid-Zeitschrift. Springer-Verlag; 2005 Nov;69(2):155–64.

74. Gennes PG de. Conformations of polymers atached to an interface. Macromolecules. Academic Press; 1980;(327):1069–75.

75. Wassel E, Wesner D, Schönherr H. Colloidal force probe study of poly(di(ethylene glycol)methylether methacrylate) homopolymer brush layers in aqueous media at different temperatures. Eur Polym J. Pergamon; 2017 Apr 1;89:440–8.

76. Stan G, Delrio FW, MacCuspie RI, Cook RF. Nanomechanical properties of polyethylene glycol brushes on gold substrates. J Phys Chem B. 2012;116(10):3138–47.

77. Nicholas AR, Scott MJ, Kennedy NI, Jones MN. Effect of grafted polyethylene glycol (PEG) on the size, encapsulation efficiency and permeability of vesicles. Biochim Biophys Acta - Biomembr. 2000;1463(1):167–78.

78. Fang C, Shi B, Pei Y-Y, Hong M-H, Wu J, Chen H-Z. In vivo tumor targeting of tumor necrosis factor-α-loaded stealth nanoparticles: Effect of MePEG molecular weight and particle size. Eur J Pharm Sci. Elsevier; 2006 Jan 1;27(1):27–36.

79. Tanwir K, Tsoukanova V. Lateral distribution of a poly(ethylene glycol)-grafted phospholipid in phosphocholine monolayers studied by epifluorescence microscopy. Langmuir. American Chemical Society; 2008 Dec 16;24(24):14078–87.